# The sensitivity of the next generation of lunar Cherenkov observations to UHE neutrinos and cosmic rays

C.W. James[1], R.J. Protheroe[2]
Department of Physics, The University of Adelaide, Adelaide, SA 5005, Australia

**Abstract**

We present simulation results for the detection of ultra-high energy (UHE) cosmic ray (CR) and neutrino interactions in the Moon by radio-telescopes. We simulate the expected radio signal at Earth from such interactions, expanding on previous work to include interactions in the sub-regolith layer for single dish and multiple telescope systems. For previous experiments at Parkes, Goldstone, and Kalyazin we recalculate the sensitivity to an isotropic flux of UHE neutrinos. Our predicted sensitivity for future experiments using the Australia Telescope Compact Array (ATCA) and the Australian SKA Pathfinder (ASKAP) indicate these instruments will be able to detect the more optimistic UHE neutrino flux predictions, while the Square Kilometre Array (SKA) will also be sensitive to all bar one prediction of a diffuse 'cosmogenic', or 'GZK', neutrino flux.

Current uncertainties concerning the structure and roughness of the lunar surface prevents an accurate calculation of the sensitivity of the lunar Cherenkov technique for UHE cosmic ray astronomy at high frequencies. However, below 200 MHz we find that the proposed SKA low-frequency aperture array should be able to detect events above 56 EeV at a rate about 30 times that of the current Pierre Auger Observatory. This would allow directional analysis of UHE cosmic rays, and investigation of correlations with putative cosmic ray source populations, to be conducted with very high statistics.

Keywords: UHE neutrino detection, UHE cosmic ray detection, coherent radio emission, lunar Cherenkov technique, UHE neutrino flux limits

## 1 Introduction

The origin of the UHE CR — protons and possibly atomic nuclei with observed energies above $10^{18}$ eV and up to at least $2 \times 10^{20}$ eV — has long remained a mystery. The deflection and scattering of CR trajectories in cosmic magnetic fields makes the flux of all but the highest energy CR appear isotropic with respect to the Galaxy regardless of their source, so that measurements of arrival directions cannot reliably be used for source identification. At the highest energies, the deflection is less, and this allows the possibility of 'seeing' nearby UHE CR sources. Arrival directions of UHE CR detected by the Pierre Auger experiment above $5.6 \times 10^{19}$ eV are

[1] Corresponding author, clancy.james@adelaide.edu.au
[2] rprother@physics.adelaide.edu.au

statistically correlated with positions of nearby AGN, which are in turn representative of the large-scale distribution of matter in the local universe [1]. However, the flux is extremely low, and so the nature of the sources of UHE CR within this distribution remains at present unresolved.

An alternative means of exploring the origin of UHE CR is to search for UHE neutrinos. As first noted by Greisen [2] and by Zatsepin & Kuzmin [3], cosmic rays of sufficient energy will interact (e.g. via pion photoproduction) with photons of the 2.73 K cosmic microwave background radiation (CMBR), with the resulting energy-loss producing a cut-off in the spectrum (the 'GZK cut-off') from a distance source at around $\sim 10^{20}$ eV. These same interactions produce neutrinos from the decay of unstable secondaries. Several experiments [4, 5, 6, 7] have reported UHE CR events with energies above $10^{20}$ eV, and therefore a flux of these 'cosmogenic neutrinos', or 'GZK neutrinos', is almost guaranteed.

Significant information on the CR spectrum at the sources is expected to be preserved in the spectrum of GZK-neutrinos [8] which varies significantly between different scenarios of UHE CR production. These include acceleration in the giant radio lobes of AGN, the decay of supermassive dark matter particles or topological defects, and $Z$-burst scenarios, the last of which have already been ruled out by limits placed on an isotropic flux of UHE neutrinos [9, 10]. Of course, neutrinos are not deflected by magnetic fields, and so should point back to where they were produced, with even a single detection allowing the possibility of identifying the source of UHE CR. See refs. [11, 12] for recent reviews of UHE CR production scenarios and radio techniques for high-energy cosmic ray and neutrino astrophysics. Here we emphasize that in all models of UHE CR origin, we expect a flux of UHE neutrinos.

UHE neutrino astronomy will be able to provide much needed clues to the origin of the UHE CR, as would a method to vastly increase the number of observed CR at UHE. In Section 2, we describe the lunar Cherenkov technique, which allows both UHE neutrino and CR detection by observing the Moon using Earth-based radio-telescopes. Section 3 details our simulation, which we use to review observational methods in the light of the next generation of radio instruments in Section 4. We calculate the effective apertures of past and future experiments in Section 5, and use these to place limits on an isotropic flux of UHE neutrinos from past experiments in Section 6. For the next generation of telescopes, we calculate the sensitivity to, and predict neutrino event rates expected for, various models of an UHE neutrino flux (Section 7), and the event rates from the (known) cosmic ray flux (Section 8). Our results and future improvements are discussed in Section 9.

# 2 The Lunar Cherenkov Technique

A high-energy particle interacting in a medium will produce a cascade of secondary particles, which develops an excess negative charge by entrainment of electrons from the surrounding material and positron annihilation in flight. The charge excess is roughly proportional to the number of particles in electromagnetic cascades, which in turn is roughly proportional to the energy deposited by the cascade. Askaryan [13] first noted this effect and predicted coher-

ent Cherenkov emission in dense dielectric media at radio and microwave frequencies where the wavelength is comparable to the dimensions of the shower. At wavelengths comparable to the width of the shower, the coherent emission is in a narrow cone about the Cherenkov angle $\theta_C = \cos^{-1}(1/n)$ ($n$ the refractive index), while for wavelengths comparable to the shower length, the coherent emission is nearly isotropic. This Askaryan effect has now been experimentally confirmed in a variety of media [14, 15, 16], with measurements of the radiated spectrum agreeing with theoretical predictions (e.g. ref. [17]). If the interaction medium is transparent to radio waves, the radiation can readily escape from the medium and be detected remotely. Since the power in coherent Cherenkov emission is proportional to the square of the charge excess, i.e. to the square of the energy deposited, extremely high energy showers should be detectable at very large distances.

The Lunar Cherenkov technique, first proposed by Dagkesamanskii and Zheleznykh [18], aims to utilise the outer layers of the Moon (nominally the regolith, a sandy layer of ejecta covering the Moon to a depth of ~10 m) as a suitable medium to observe the Askaryan effect. Since the regolith is comparatively transparent at radio frequencies, coherent Cherenkov emission from sufficiently high-energy particle interactions (specifically, from UHE cosmic ray and neutrino interactions) in the regolith should be detectable by Earth-based radio-telescopes. First attempted by Hankins, Ekers & O'Sullivan [19] using the Parkes radio telescope, subsequent experiments at Goldstone (GLUE) [9] and Kalyazin [20] have placed limits on an isotropic flux of UHE neutrinos. Observations continue at both Westerbork (WSRT) [21] and the Australia Telescope Compact Array (ATCA; our project), and the technique has been the subject of several theoretical and Monte Carlo studies [22, 23, 24, 25] together with our own recent work [26].

Future radio instruments will provide large aperture array (AA) tile clusters and arrays of small dishes with very broad bandwidths, with both factors allowing very strong discrimination against terrestrial radio frequency interference (RFI). The culmination of the next generation of radio instruments will be the Square Kilometre Array (SKA), to be completed around 2020, with smaller pathfinders such as ASKAP (Australian SKA Pathfinder [27]) to be built in the intervening period. In the meantime, our project aims to perform a series of experiments with the Australia Telescope Compact Array (ATCA), an array of six 22 m dishes currently undergoing an upgrade to an eventual 2 GHz bandwidth. Lunar Cherenkov experiments with these instruments, together with those proposed for LOFAR [21], represent the foreseeable future of the technique.

# 3 Description of Modelling

Our simulation method is the same as that developed in a previous paper [26] to simulate the detection of UHE neutrinos by the Parkes lunar Cherenkov experiment of Hankins et al. [19], and except where we explicitly state otherwise, the simulation methods for both papers are identical. The simulation uses Monte Carlo methods, generating UHE particles incident on the Moon at discrete energies, with lunar impact parameter $r$ sampled with $p(r) \propto r$ for $0 < r < r_m$,

the lunar radius. The Moon was approximated to be spherically symmetric, with the density being constant within zones as given in Table 1, the outer two layers being the sub-regolith (see Section 3.2) and the regolith.

We assume equal proportions of $\nu_e, \nu_\mu, \nu_\tau$, since we expect oscillations to result in complete flavour mixing over extragalactic distance scales [28]. Neutrinos and anti-neutrinos are treated identically throughout the simulation. Cross-sections for both charged-current (CC) and neutral-current (NC) interactions are taken from Gandhi et al. [29], with the interaction inelasticity $y$ (fraction of neutrino energy given to hadronic showers — see Section 3.3) sampled from the distributions used by Beresnyak [25]. The $\mu/\tau$ generated in $\nu_\mu, \nu_\tau$ CC interactions are discarded, since their bremsstrahlung energy-loss rate will be insufficient to begin detectable cascades. We ignore photo-hadronic interactions (which allow high-energy bremsstrahlung photons to convert some of the shower energy into hadronic cascades), so that the $e^\pm$ from $\nu_e$ CC interactions are assumed to produce purely electromagnetic showers. Unless the $e^\pm$ emits a bremsstrahlung photon with a significant fraction of its initial energy, any secondary hadronic showers from photo-hadronic interactions will be both of low energy and strung out along the shower length, so that the whole showers appears similar to a purely electromagnetic one. Since $\nu_e$ CC interactions form approximately only two ninths of all primary neutrino interactions, and most $e^\pm$ thereby produced will not emit such a high-energy photon, this simplification is justified.

Interactions are treated as point-sources of coherent Cherenkov radiation, with the Cherenkov cone axis being in the direction of the incoming particle. We parameterise the radiation spectrum as described in Section 3.3, with radiation spectra from the coincident hadronic and electromagnetic showers in $\nu_e$ CC interactions calculated separately. We propagate the radiation using ray-tracing, treating boundaries between media as infinite plane interfaces. Transmission of the radiation at these boundaries is calculated from the Fresnel transmission coefficients for each component of the polarisation, and the solid-angle-stretching factor applicable to radiation from a point source. We also account for both large-scale surface roughness (Section 3.1), and absorption (Section 3.2).

## 3.1 Treatment of Surface Roughness

The frequency range of the experiments to be modelled is large, and since the lunar surface is rougher on small length scales than on large scales the surface will appear smoother at longer wavelengths. We use the RMS unidirectional slope $S_{\mathrm{rms}}$, i.e. the RMS of slopes measured along arbitrary vertical plane sections through of the surface, based on measured values appropriate to the observation wavelength of the lunar Cherenkov experiment in question. Shepard et al. [30] model the dependence of $S_{\mathrm{rms}}$ on the wavelength as a power-law, finding the relation between the wavelength $\lambda$ (in cm) and the slope tangent given in Eqn. 1:

$$\tan S_{\mathrm{rms}} = 0.29\lambda^{-0.22} \quad (1)$$

Somewhat confusingly, it is in fact the tangent of $S$ which is normally distributed (as opposed to $S$ itself), i.e. $\tan S$ is sampled from a normal distribution with mean 0 and standard deviation

tan $S_{\rm rms}$, though convention dictates that $S$ has the RMS subscript. In the simulation, the surface normal at some location is determined as follows: (i) two orthogonal vertical planes are chosen to intersect with each other and the nominal spherical lunar surface at the chosen location, (ii) a line through the intersection point is constructed in each orthogonal plane, each having a slope sampled from the distribution above, (iii) the local surface is deemed to be the surface containing both these lines. Throughout we use Eqn. 1 with the central frequency $\sqrt{f_1 f_2}$ of the frequency range $f_1$ to $f_2$ of the observations to simulate the roughness of the lunar surface. We repeat the caution of our earlier paper [26] that this simulates only the effects of large-scale surface roughness (e.g. from sizeable craters) illustrated in Fig. 1(a), and approximates the effects of small-scale surface roughness illustrated in Fig. 1(b) by using values of $S_{\rm rms}$ at the scale corresponding to the wavelength of the observations. In the case of the Parkes experiment, with a central frequency of 1.4 GHz and a bandwidth of 500 MHz, Eqn. 1 predicts $S_{\rm rms} \approx 8.5°$. In our earlier work we used $S_{\rm rms} = 6°$, and given that Beresnyak [25] found that increasing the surface roughness, i.e. increasing $S_{\rm rms}$, led to a larger effective aperture, the effective aperture for the Parkes experiment calculated here will thus be greater than that in ref. [26].

To model cosmic rays, the procedure is similar to that for neutrinos, except that CR are assumed to interact immediately at the surface, with 100% of the energy going into hadronic showers. Current methods (including ours) of generating $S_{\rm rms}$ are not really appropriate for cosmic ray interactions, since correlations between local surface features (which will be transparent to neutrinos) and the position of cosmic ray interaction are ignored. As illustrated in Fig. 2, cosmic rays will tend to interact with unfavourable surface slopes, as in the right-hand side of the hill in the figure, with the surface normal pointing back towards the particle arrival direction. For such geometries, only radiation far from the Cherenkov cone will be able to escape total internal reflection, and the experimental aperture will be reduced, particularly at high frequencies. One limit (a 'worst-case' limit) of this effect can be made by always generating the surface normal in the half-hemisphere pointing back towards the arrival direction of the incident particle, while a 'best-case' estimate comes from ignoring correlations and generating the surface normal as with neutrinos. We only consider our estimates of the aperture to UHE CR reliable if the results of these two methods converge — where they diverge, a more thorough treatment will be necessary. As found by Scholten et al. [31], the suppression of radiation from showers developing close to the surface (formation zone effect – see [24]) is expected to be negligible even at low frequencies where the effect will be greatest, so we ignore this effect. Note, though, that this suppression is effectively included in the worst-case limit above, since this method considerably lowers the probability of generating a shower developing nearly parallel (and hence close) to the surface.

## 3.2 Treatment of the Sub-Regolith Layer

In our previous simulation, the medium in which Cherenkov radiation is produced and transmitted to the lunar surface was modelled only as a single surface layer, nominally the regolith, with density $\rho = 1.8$ g cm$^{-3}$. Since the regolith is formed from impact ejecta, the composition of the regolith — and hence its dielectric properties — should reflect that of the local under-

lying material (substrate). As discussed by Wilcox et al. [32], what constitutes the boundary between the regolith and the substrate is poorly defined, since changes in density (increasing with depth) and the degree of rock fragmentation (decreasing with depth) are expected to be smooth. Neither of these should qualitatively affect the usefulness of the substrate as a dense radio-transparent medium. Ignoring the sub-regolith layers artificially limits the aperture, except to low-energy events for experiments observing at high frequencies, as interactions in the substrate would otherwise be detectable at low frequencies or high energies. Therefore, we modify our simulation as described below to allow interactions in a substrate layer to produce detectable coherent Cherenkov radiation. Although such a layer has been previously modelled (as an extended, uniform regolith of 500m depth) [21], in our present work we treat the layers separately, and develop our own model as described below.

In the Mare, the substrate medium is cooled lava, while in the highlands, it is the megaregolith. At our current (low) level of sophistication, a uniform model for both is justified. Our model, requiring a mean depth and density, dielectric properties, Cherenkov radiation parameterisation, and a method to propagate radiation from the substrate to the regolith, should be more representative of the megaregolith than Mare basalt, since highland terrain is dominant. We model the substrate and the $r > 1670$ km layer (nominally the crust, of density 3 g/cm$^3$ — see Table 1) as essentially the same medium, which we assume to begin at a depth of 10 m. This density is possibly an overestimate, since the substrate is unlikely to be as dense as the (underlying) crust, and models for a dual-layer crust (here we use a single layer) find a lower density for the upper portion [33].

We use the results of Olhoeft & Strangway [34] to scale both the refractive index $n$ and attenuation length $\ell$ of the substrate from the measured values of the regolith. These authors obtained the density-dependence of both $n$ and $\ell$ at frequencies ranging from 100 kHz to 9 GHz using results on soil samples and rock fragments from both Mare and highlands regions. They also found that the attenuation length depended on the fraction of iron and titanium present. While there is evidence of an increased iron content at depths greater than ~8 km, no variation at shallower depths has been observed except from Mare basalts [35]. Therefore we scale the values of $n = 1.73$ and $\ell = 60\ \lambda$ (with $\lambda$ the wavelength in a vacuum, i.e. $\lambda = c/f$) used for the regolith in our previous paper [26] solely with the density as per Olhoeft & Strangway, obtaining $n = 2.5$ and $\ell = 29\ \lambda$ for a density of 3 g/cm$^3$. The depth is modelled as being essentially infinite, since even at 100 MHz the attenuation length of 87 m is small compared to the estimated 2 km mean depth of the substrate [36, 37]. We believe that our model of the sub-regolith layer is an adequate reflection of reality, and except where otherwise noted include such a layer. Since the nature of the sub-regolith is poorly constrained by measurement we also run our simulation with this layer excluded, and it is feasible that our results for a single shallow layer of regolith will prove to be the more accurate.

The interface between the sub-regolith and regolith is treated using ray-tracing as a standard refraction problem at a plane boundary, on the assumption that the slope of the boundary is the same as the slope at the surface. This assumption reflects the likely situation in the Mare, where the lava flows are expected to present a solid (if fractured) interface. In the highlands, the less distinct transition from regolith to sub-regolith will appear more like the model of a sharp

interface between uniform media at low frequencies, and so will be less sensitive to inhomogeneities (e.g. rock fragments) in the transition region. At high frequencies, the contribution to the expected event rate from events below the regolith will be minor due to absorption in the upper regolith layer, suggesting our approximation is not inappropriate. We await the results from instruments such as the lunar radar sounder [38] on-board SELENE [39] to enable our model to be improved.

## 3.3 Modelling Cherenkov Emission

To calculate the spectrum of observed Cherenkov radiation, we use the parameterisation developed in our previous paper [26]. This combines results from numerous different papers, in some cases scaled from ice to the regolith and/or from low to high energies. Since here we also scale the parameterisation from the regolith to the sub-regolith, in the interest of clarity, we fully detail all the formula used.

In UHE neutrino-nucleon interactions, the struck nucleon initiates a hadronic cascade taking typically ~20% of the incident neutrino's energy. In neutral current (NC) interactions, the remaining ~80% of the energy goes to the scattered neutrino which contributes no Cherenkov radiation. However, in charged current (CC) interactions, a $\mu$, $e$ or $\tau$ is produced taking the remaining ~80% of the energy. A singly-charged $\mu$ or $\tau$ will contribute negligible Cherenkov radiation, while an electron will initiate an electromagnetic (EM) cascade. Thus for neutrinos of energy $E_\nu$ there will be a hadronic shower of energy $E_S \approx 0.2E_\nu$, and in the case of electron-neutrino CC interactions there will also be an EM shower of energy $E_S \approx 0.8E_\nu$. However, such showers will be substantially lengthened due to the Landau-Pomeranchuk-Migdal (LPM) effect, with radiation emitted in a correspondingly narrow cone, so that at very high energies the electromagnetic cascade will actually contribute less coherent radiation than the hadronic cascade at most observation angles. For cosmic rays of energy $E_{CR}$ the shower energy is simply $E_S = E_{CR}$.

The field strength $\mathcal{E}_{\rm EM}(\theta_C, f)$ (V/m/MHz) at distance $R$ (m) from electromagnetic showers for radiation emitted at angle $\theta = \theta_C$ from the shower axis is given by:

$$R|\mathcal{E}_{\rm EM}(\theta_C, f)| = V_0 \times \left(\frac{E_S}{1\ \text{EeV}}\right)\left(\frac{f}{1\ \text{GHz}}\right)\left(\frac{1}{1+(f/f_0)^\alpha}\right) \quad \text{(V/MHz)} \tag{2}$$

where $f$ is the frequency and $E_S$ is shower energy in EeV (1 EeV $\equiv 10^{18}$ eV), and $\alpha$ depends on the medium.

The amplitude of coherent Cherenkov radiation from hadronic showers is related to that of electromagnetic showers by

$$\mathcal{E}_H(\theta_C, f) = f(\epsilon)\,\mathcal{E}_{\rm EM}(\theta_C, f) \tag{3}$$

where $f(\epsilon)$ describes the fraction of energy going into electromagnetic sub-showers, and $\epsilon = \log_{10}(E_S/1\ \text{GeV})$. The result for ice [40] is

$$f(\epsilon) = -1.27\times10^{-2} - 4.76\times10^{-2}\epsilon - 2.07\times10^{-3}\epsilon^2 + 0.52\sqrt{\epsilon}. \tag{4}$$

The function $f(\epsilon)$ is largely determined by the rate of neutral pion production in hadronic interactions, since neutral pions decay into electromagnetic products. Variation in $f(\epsilon)$ is therefore expected between media due to different hadronic interaction cross sections of the target nuclei. At very high energies however, the variation is less, and the dominant source of error comes from uncertainties in the hadronic interaction models [41]. Hence Eqn. 4 is used unmodified for both the regolith and sub-regolith.

Away from the Cherenkov angle, the emission falls off due to decoherence over the width and length of the shower track. This can be approximated by

$$\mathcal{E}(\theta, f) = \mathcal{E}(\theta_C, f) \left(\frac{\sin\theta}{\sin\theta_C}\right) 2^{-(\theta-\theta_C)^2/(\Delta\theta)^2}. \quad (5)$$

The $\sin\theta$ dependence becomes significant at low frequencies, where $\Delta\theta$ is large. We use $\Delta\theta$ given by Alvarez-Muñiz et al. for electromagnetic [42] and hadronic [40] showers, scaling the hadronic result above $10^{19}$ eV as per Williams [43]. For hadronic shower energies above 10 EeV, and for electromagnetic showers of all energies considered here,

$$\Delta\theta_H = C_{\rm H}\left(\frac{f}{1\ {\rm GHz}}\right)^{-1} \frac{1}{1 + 0.075\log_{10}(E_S/10\ {\rm EeV})} \quad (6)$$

$$\Delta\theta_{\rm EM} = C_{\rm EM}\left(\frac{f}{1\ {\rm GHz}}\right)^{-1} \left(\frac{E_{\rm LPM}}{0.14E_S + E_{\rm LPM}}\right)^{0.3} \quad (7)$$

where $E_{\rm LPM}$ is the energy above which the LPM effect becomes important. See Eqn. 6 of Alvarez-Muñiz et al. [40] for the (rather complex) parameterisation of $\Delta\theta_H$ for $E_S < 10$ EeV showers — in our notation, the factor of 1° in this equation becomes 0.7° $C_H$, and $\nu_0/\nu$ becomes 1 GHz/ $f$.

The constants $V_0$, $C_H$, $C_{\rm EM}$, $f_0$, $\alpha$ and $E_{\rm LPM}$ are medium-dependent, with only $E_{LPM}$ calculated explicitly for a given composition [44]. Alvarez-Muñiz et al. [45] found the variation of $\alpha$ between media to be low, and since $\mathcal{E}$ is insensitive to changes in $\alpha$ at frequencies below $f_0$, we adopt the value found by the authors for the regolith ($\alpha = 1.23$) also for the sub-regolith. Alvarez-Muñiz et al. [45] also used a 'box' model of shower development to predict changes in $V_0$ and parameters related to $C_{\rm EM}$ and $f_0$ for regolith, given values for ice, and compared these predictions to the values found from full regolith simulations. Variation in all parameters except $V_0$ is satisfactorily explained by this model, with a 30% discrepancy between the scaled and simulated values of $V_0$. This is probably due to the different composition of the regolith when compared to ice, which would alter the cross-sections at low-energy for processes in the electromagnetic cascade, the rate of interactions producing excess track length, and hence the intensity of coherent Cherenkov radiation. Therefore we expect a more accurate scaling of $V_0$ from the regolith to sub-regolith which have identical compositions, and hence changes predicted by the box model in all electromagnetic shower parameters between the regolith and substrate are expected to be reliable. Since the emission from hadronic showers comes from low-energy electromagnetic cascades, we scale both types of shower identically.

For the above box-model of shower development, the magnitude of Cherenkov radiation at the Cherenkov angle is proportional to $\sin\theta_C/\rho$, where $\rho$ is the density, with both the width of

the Cherenkov cone $\Delta\theta$ and turnover frequency $f_0$ being proportional to $\rho/\sqrt{n^2-1}$ [45]. Using this model, with 'R' indicating regolith and 'SR' sub-regolith, and given $\theta_C^{\mathrm{SR}} = 66.4°$, we expect $V_0^{\mathrm{SR}} = 0.67\,V_0^{\mathrm{R}}$, and both $\Delta\theta^{\mathrm{SR}} = 1.027\Delta\theta^{\mathrm{R}}$ and $f_0^{\mathrm{SR}} = 1.027\,f_0^{\mathrm{R}}$. Also, the LPM energy is lower in the sub-regolith due to its higher density. Table 2 details the relevant constants for both layers. The scaling of these parameters with $\rho$ (since $n = n(\rho)$) means that a higher sub-regolith density results in a lower effective aperture for lunar Cherenkov experiments, even once the increased neutrino interaction rate in a denser medium is accounted for. The main uncertainty is expected to be due to our limited knowledge of the structure of the sub-regolith.

## 3.4 Modelling Neutrino Detection Experiments

To model the GLUE and Kalyazin experiments, we use similar methods to that for Parkes [26]. We assume Airy beam patterns, with angular widths calculated from the physical diameters of the antenna, and estimate the noise in each data channel / frequency band, assuming a lunar temperature of 225° K [46] and base (or 'cold-sky') system temperature of 35° K. This method reproduces well the system temperatures for the past experiments where reported. For the GLUE experiment, we simulate the full five-fold coincidence detection algorithm (as implemented for most of the experiment), with a detection requiring an event to be above the thresholds specified in Williams [43] in all five data channels. The simulation for the Kalyazin experiment is somewhat simpler, needing only to model a singly-triggered data channel. See Gorham et al. [9] and Beresnyak et al. [20] for details of these experiments.

It is beyond the scope of this paper to perform a full optimisation of observation parameters for future experiments with ATCA, ASKAP, or SKA. To calculate detection thresholds, we use dual circularly polarised data channels with thresholds of $V_{\mathrm{thresh}} = 6\,V_{\mathrm{rms}}$ in coincidence, with $V_{\mathrm{rms}}$ calculated as for previous experiments, and cold-sky system temperatures of 30° for ATCA [47] and an assumed value of 35° K for ASKAP and SKA. Dispersion in the ionosphere is assumed to be corrected for prior to triggering (i.e. we ignore it), as is beam-forming adequate to cover the entire Moon with the full collecting area. While this last assumption is overly optimistic, even for the small number of baselines provided by ATCA or the expected processing power of the SKA, the full sensitivity in each case may be recovered by using a lower trigger threshold off the central core, and writing buffered data from outlying stations upon triggering.

For reasons outlined below (Section 4), future detection algorithms should search for lunar Cherenkov pulses in multiple frequency ranges. While for this one pays a statistical penalty in sensitivity, even a 10-fold increase in statistical trials can be compensated for by a very small sensitivity loss, e.g. by instead using $V_{\mathrm{thresh}} = 6.2\,V_{\mathrm{rms}}$. For ATCA, ASKAP, and the SKA, we therefore model a range of frequencies and bandwidths using 50 MHz intervals, and choose the experimental sensitivity to be the highest at a given energy. Bandwidth limitations are set by the frequency range of the instruments, except in the case of ASKAP, with a maximum bandwidth of 300 MHz. In the case of the SKA, multiple systems will be utilised to cover the very broad frequency range [48]. Here we assume three: a sparse aperture array (AA) at the lowest frequencies (AA low), a dense AA at higher frequencies (AA high), and dishes for the highest frequencies. We model the sensitivity separately for each, reflecting the likely technological

constraints of combining the signals from multiple arrays into a single coherent beam. Table 3 outlines the assumed specifications used to model the capabilities of these instruments.

# 4 Observational Phenomenology

The current designs of next-generation radio-instruments are sufficiently different to that of instruments previously used for lunar Cherenkov observations to warrant a new investigation of optimal observational parameters. Here we examine the effects of pointing position and bandwidth, and explicitly establish some results which have so far been implicit in the design of future lunar Cherenkov observations.

## 4.1 Broad Bandwidth Observations

Experiments at Parkes, and in particular Goldstone and Kalyazin, have operated in the regime where bandwidth $\Delta f$ is small compared to the observation frequency $f$, so that both signal field-strength and noise power scale linearly with the bandwidth. Therefore, the received signal-to-noise power scales linearly with $\Delta f$, and increasing $f_{\max}$ or decreasing $f_{\min}$ both equally increase the effective aperture to particles of all energies.

This is no longer the case once the bandwidth becomes comparable to the observation frequency (i.e. $\Delta f \not\ll f$), so that the signal strength of lunar pulses, and band noise from either the galactic background (low frequencies) or lunar thermal emission (high frequencies), may change appreciably over the bandwidth. In this regime, sensitivity to geometrically-favourable events (shallow interactions viewed near the Cherenkov angle) will be increased by extending the bandwidth to higher frequencies, since coherency from such events could extend beyond 3 GHz. However, most geometrically unfavourable events will be drowned out by the resulting increase in band noise, since (due to regolith absorption and/or decoherence) these events will not have a significant high-frequency signal. To demonstrate this effect, we calculate the effective area to UHE neutrinos from a fictitious instrument of effective area $50,000$ m$^2$ and system temperature 50 K (neglecting both lunar thermal emission and the galactic background noise), covering the Moon uniformly in beams. We run simulations over a variety of bandwidths $\Delta f$, both for fixed $f_{\min}$ (= 100 MHz) and fixed mean frequency $\bar{f} = (f_{\max} + f_{\min})/2$ (= 1 GHz). In Fig. 3, we show contour plots in the $E_\nu$–$\Delta f$ plane of the aperture $A(E_\nu, \Delta f)$ at each energy/bandwidth divided by the peak aperture for that energy — (a), for fixed $f_{\min}$; (b), for fixed $\bar{f}$.

The fixed-$f_{\min}$ plot (Fig. 3(a)) clearly shows that for decreasingly low energy neutrinos, the peak aperture is achieved with an increasingly high $f_{\max}$ and a broader bandwidth (e.g. $\Delta f > 1$ GHz for $E_\nu < 10^{20}$ eV), since only geometrically-favourable events are detectable at all. Too low an $f_{\max}$ results in an aperture of zero. At higher energies, the vastly more common geometrically-unfavourable events become detectable, and the optimum bandwidth reduces to below 100 MHz. Importantly, the decline in aperture by increasing $f_{\max}$ above the optimum is slower than by reducing it below (i.e. the contours are closer together for low bandwidths), even in log-space. Increasing $f_{\max}$ results in a ~linear increase in noise power, since noise adds

incoherently, so the loss of signal-to-noise through having $f_{max}$ too high is small. However, since the signal is coherent, with $\mathcal{E}(f)$ rising as steeply as $f$, the rate of loss of peak signal power by decreasing $f_{max}$ can be up to cubic. Also, at the highest energies, events appearing only at low frequencies are generally strong enough to be detected over the increased noise introduced by a high $f_{max}$. Thus the reduction in effective aperture for a lower than optimal $f_{max}$ is worse than for a higher than optimal $f_{max}$.

The fixed-$f$ plot (Fig. 3(b)) is somewhat deceptive, and illustrates why in this paper we use $f_{min}$, $f_{max}$ rather than $f, \Delta f$ to describe bandwidths. At first glace, the figure seems to imply that large bandwidths are ideal at all energies, which, for a fixed $f$, is certainly true. However, in the high-energy regime, the very strong bandwidth-dependence is due entirely to the rapid relative variation of $f_{min}$ as $\Delta f \to 2f$, because of the aforementioned detection over a large bandwidth at high energies of strong signals appearing only at low frequencies. This depends not so much on $f_{max}$ but on $f_{min}$, which if too high will exclude such events altogether. However, if the energy is sufficiently low that such events are undetectable, the effect of increasing bandwidth for fixed $f$ is low also, explaining why the bandwidth-dependence is less at low energies.

## 4.2 Optimum Pointing Position

As first reported by Gorham et al. [49] for GLUE, the greatest sensitivity to UHE neutrinos for previous experiments has been achieved when pointing at the lunar limb, partly because the majority of signals are expected to come from the limb, and partly because pointing at the limb reduces the lunar thermal emission received by a detector, thus also reducing the detection threshold. Both effects become important when the beam size is comparable to or smaller than the Moon's angular diameter of $\sim 0.5°$. Obviously, if the beam illuminates the Moon's surface uniformly, the origin of the signals on the lunar surface does not affect the probability of detection. This is also the case in experiments which can form multiple independent beams, e.g. by the use of focal plane arrays (FPAs).

To model the effects of changing beam size and pointing position, we simulate the same fictitious instrument as above, but vary the antenna diameter from 8 to 256 m while keeping the total effective collecting area of the instrument constant (i.e. we vary the number of antennas), and add the contribution of lunar thermal emission to the base system temperature. We (somewhat arbitrarily) use an observation frequency of 1 GHz, with a narrow 100 MHz bandwidth to remove the aforementioned broad-bandwidth effects.

Our results for $E_\nu = 10^{20}$ eV and $E_\nu = 10^{22}$ eV are plotted in Fig. 4. For all energies and pointing positions, using a larger number of smaller dishes increases the effective aperture. Smaller dishes have greater coverage of the lunar surface, due to a larger individual beam size, *and* an increased sensitivity, since the lunar thermal emission is largely incoherent between individual dishes. This is one of the main reasons why ATCA ($6 \times 22$ m dishes) is a potentially superior instrument over Parkes ($1 \times 64$ m dish), despite a similar collecting area. Note that in a real experiment, lunar thermal emission would be partially correlated between individual antenna. This would increase thermal noise beyond that calculated, especially for closely-packed small antennas, thus decreasing their advantage. Also, the processing requirements

of beamforming over the entire lunar solid angle for many individual antennas are large, which is of course why instruments with a large number of individual small elements (the 'large $N$, small $d$' concept) are only now being developed.

For large antenna at low energies, pointing at the limb results in a net gain in aperture, both because the slight reduction in threshold from reduced lunar noise results in a large increase in detectable events, and because events far from beam centre (i.e. events on the limb when in centre-pointing mode) are in any case undetectable. At high energies, the number of events lost from the far limb is greater than that gained from the near, while the change in sensitivity matters little since events are energetic enough to be readily detectable.

With these qualitative conclusions established, we now proceed to calculate the effective apertures for both past and future experiments.

# 5 Effective Aperture of Past and Future Experiments

In Fig. 5 we plot the effective aperture, $A(E_\nu)$ (km$^2$ sr), to neutrinos of previous experiments, both with (Fig. 5(a)) and without (Fig. 5(b)) the sub-regolith layer. For these >GHz observations, the contribution to the effective aperture from interactions in the sub-regolith dominates only above $\sim 10^{22}$ eV, and so the dependence of our revised limits on the nature of the sub-regolith is only significant at energies where some models predicting large fluxes have already been ruled out [10]. As we noted earlier [26], the effective aperture we calculate for GLUE with the sub-regolith excluded is significantly less than that estimated under similar assumptions by Gorham et al. [9]. For reasons we have noted earlier [26], the GLUE and Kalyazin simulations appear inconsistent with each other, and our result for the effective aperture of the Kalyazin experiment is in good agreement with that calculated by Beresnyak et al. [25], after allowing for the greater regolith depth (30 m) and lower threshold used.

The predicted effective apertures $A(E_\nu)$ for future experiments is shown in Fig. 6. Except in the case of ASKAP (with a comparatively small bandwidth of $\Delta f \approx 0.3\, f$), the greatest apertures at the highest energies were indeed achieved by using only a fraction of the available bandwidth, e.g. for the SKA dishes, a full bandwidth of 0.7-3.0 GHz was optimum for neutrino energies at and below $2 \times 10^{18}$ eV only, while above $10^{21}$ eV, the greatest aperture is achieved over a 200 MHz bandwidth (from 0.7-0.9 GHz). In all cases, the dependence of the optimal bandwidth for a given experiment on the inclusion or otherwise of the sub-regolith layer was very slight, even while the dependence of $A(E_\nu)$ was very strong.

Given the large increase in sensitivity offered by the SKA, the order-of-magnitude reduction in the neutrino-energy detection threshold over possible experiments with ATCA and ASKAP appears low, though these in turn offer an order-of-magnitude threshold reduction over the experiments at Parkes, Glue, and Kalyazin. Reducing this threshold in an experiment utilising coherent Cherenkov radiation is so difficult because the emitted power scales as the square of the shower energy, and the interaction rate as $E_\nu^{0.363}$. The low interaction rate however means that at $10^{19}$ eV, an aperture of 1 km$^2$ sr is equivalent to an effective volume of approximately 40 km$^3$ water-equivalent seeing all $4\pi$ sr. We therefore assess the utility of these experiments in

the context of expected event rates from and potential limits on an UHE neutrino flux.

# 6 Neutrino Limits from Past Experiments

Limits from past experiments have either been expressed as a 'model-independent' limit as per [50] or as a limit on a (typically) $dN/dE \propto E^{-2}$ flux between two energies — we favour the former method, since the resulting limit reflects the energy-dependence of the effective experimental aperture. In the case of a non-detection, the corresponding limit is $s_{\rm up}/[t_{\rm obs}A(E_\nu)]$, with $t_{\rm obs}$ the observation time, and the statistical factor for an upper bound $s_{\rm up}$ at 90% confidence is 2.3 (in the sole case of FORTE, $s_{\rm up} = 3.89$ for one uncertain event). Existing limits, summed over neutrino flavour, on an isotropic, uniform-flavour flux of UHE neutrinos are plotted in Fig. 7. Over the $10^8$–$10^{15}$ GeV energy range, the strongest limits come from IceCube [51], RICE [52], ANITA-lite [10] and FORTE [50]. Our revised estimates for the limits from GLUE, Kalyazin, and Parkes are now of mostly historical significance, with our limit for GLUE being approximately an order of magnitude higher (i.e. less limiting) than given in [9], reflecting our lower estimate of the GLUE effective aperture.

For the projected ANITA limits [10], we scale the published 50-day sensitivity estimates to the 18 day duration of their December 2006 balloon flight, and convert to a 90% confidence model-independent limit by multiplying by 2.3 because of presumed non-detection – we await with interest the publication of the 2006 result.

# 7 Flux Predictions and Future Experiments

We shall first consider the diffuse UHE neutrino intensity predicted in various models, and then the sensitivity and expected event rate for future experiments.

## 7.1 UHE neutrino predictions and expected event rates

In Fig. 8, we plot the region excluded by past experiments (shaded area) together with a range of predicted UHE neutrino fluxes which should be detectable by future experiments. First we consider models of GZK neutrinos. Being the only guaranteed source of UHE neutrinos we shall give a fairly detailed summary of flux predictions. The assumptions in all cases are that the UHE CR are extragalactic, and accelerated with a power-law spectrum $E^{-\alpha}$ up to some maximum energy $E_{\rm max}$, often with an exponential cut-off (see [8] for a discussion of cut-offs and pile-ups in spectra of accelerated particles). Furthermore the cosmic ray power is assumed to evolve with redshift $z$, usually in a similar way to the star formation rate or quasar luminosity function. Cosmic rays are propagated through the CMBR by Monte Carlo or other means taking account of the $z$-dependence of the CMBR and other target fields, and their flux at $z = 0$ is obtained by weighting with the cosmic ray power evolution model, and integrating of redshift taking account of cosmological expansion. The resulting UHE CR flux is normalized to the observed spectrum, and the same normalization factor is applied to the GZK neutrino flux resulting

from the same calculation. In the case of a mixed composition, i.e. protons plus heavy nuclei, it is reasonable to assume that if protons are accelerated to $E_{\rm max}$, then nuclei are accelerated to $ZE_{\rm max}$ where $Z$ is the atomic number. Generally, the trend is that the higher the maximum energy and the flatter the spectrum on acceleration, the higher the GZK neutrino flux. Also, models with strong evolution of cosmic ray source power with redshift tend to give a higher GZK neutrino flux.

One such calculation was made by Protheroe & Johnson [53] of the GZK neutrino flux expected for the case of UHE CR acceleration in Fanaroff-Riley II radio galaxies [54] with protons accelerated with an $E^{-2}$ spectrum to $3 \times 10^{20}$ or $3 \times 10^{21}$ eV (boundaries of shaded area in Fig. 8a labelled PJ96). More recently, a similar calculation was made by Engel et al. [55], with an $E^{-2}$ spectrum to $3 \times 10^{21}$ eV, cosmic ray source evolution of $(1 + z)^4$ to $z$=1.9 and constant for $1.9 < z$, and Einstein-de Sitter cosmology. Their result (chain curve in Fig. 8b labelled En01) was almost indistinguishable from that of Protheroe & Johnson for the same cut-off. They found that using the more recent ΛCDM cosmology the flux (solid curve in Fig. 8b labelled En01) would be about a factor of 2 higher. Even more recently, Allard et al. [56] have made calculations for a variety of spectra and compositions. We show curves labelled Al06 in Fig. 8a, all of which are for cosmic ray source evolution $(1 + z)^4$ to $z$=1 and constant for $1 < z < 6$, (i) solid curve – a mixed composition accelerated with an $E^{-2.1}$ spectrum to $Z\times3\times10^{20}$ eV, (ii) dotted curve – a mixed composition accelerated with an $E^{-2.1}$ spectrum to and $Z\times3\times10^{21}$ eV, and (iii) dashed curve – protons accelerated with an $E^{-2.4}$ spectrum to $3\times10^{20}$ eV. The mixed compositions can give rise to lower neutrino fluxes because photo-disintegration dominates for heavy primaries, and the resulting nucleons having lower energy have fewer pion photoproduction interactions from which neutrinos result. Similarly, production spectra steeper than $E^{-2}$ result in fewer neutrinos. Hence the neutrino flux predicted by Allard et al. is lower than that of Protheroe & Johnson and cuts off at lower energy. Anchordoqui et al. [57] consider a range of maximum energies, compositions and spectra. Their GZK neutrino flux is plotted for protons injected with a $E^{-2.2}$ spectrum to $4\times10^{20}$ eV and cosmic ray source evolution $(1 + z)^3$ to $z$=1.9 and constant for $1.9 < z < 2.7$ – their predicted GZK neutrino flux is significantly lower than all the other predictions of GZK neutrinos.

In addition to these GZK neutrino fluxes, we show two topological defect (TD) models, a generic TD model just allowed by gamma-ray and cosmic ray data in 1996 (Protheroe & Stanev [58]), and a more recent TD model for 'necklaces' (Aloisio, Berezinsky & Kachelreiß [59], see [60]). These are plotted in Fig. 8. In addition, we show a range of generic optically thin AGN photoproduction source models with protons accelerated to $3 \times 10^{20}$, $10^{21}$, $3 \times 10^{21}$ and $10^{22}$ eV, interpolation based on Fig. 2b of Mannheim, Protheroe & Rachen [61]. While those models with higher maximum energies may already be ruled out (on various grounds), they are included to provide some benchmarks for estimating neutrino event rates.

## 7.2 Sensitivity of Future Experiments

For future experiments, we plot the sensitivity (cm$^{-2}$ s$^{-1}$ sr$^{-1}$ GeV$^{-1}$) to the total neutrino flux over all flavours, assuming complete flavour mixing. That is, for experiments sensitive to one

flavour only, we multiply the sensitivity by 3, and for those presenting projected limits, we remove the statistical uncertainty factor $s_{up}$ by dividing by 2.3. To avoid the somewhat arbitrary choice of 'observation time' $t_{obs}$ for future experiments, we use our best estimates of the mean observation time available in one calendar year. For lunar Cherenkov observations, this corresponds to the time the Moon appears above the telescope horizon. Using a 30° elevation angle for the horizon of aperture arrays and 10° for other radio instruments gives a mean on-time fraction $\epsilon_{on}$ of 28.8% (105 days per year) and 42.6% (156 days per year) respectively for an instrument at latitude ~26.5° S (applicable to ASKAP and, the authors' personal bias hopes, the SKA), and slightly less for ATCA at 30° S. For LOFAR [21], we scale the expected limit for 30 days to 17% of a year, reflecting the high latitude (at ~52.5° N) and approximate 30° horizon, and convert to sensitivity. For the Pierre Auger fluorescence detectors (FD), with $\epsilon_{on}$ = 10%, Miele et al. [62] recently estimated the total effective aperture to tau leptons. For the Auger surface detectors (SD) [63], which operate continuously, $\epsilon_{on}$ = 100%.

The resulting sensitivities using $t_{obs} = \epsilon_{on} \times$ 1 year on an UHE neutrino flux for these experiments are plotted together with predictions of an UHE neutrino flux in Fig. 8. Note that our sensitivity estimates for the SKA are less than previous estimates submitted to 'Square Kilometre Array Design Studies' [64]. This is due to a combination of changed assumptions about the SKA's sensitivity (particularly for the low-frequency AA), the use of three independent technologies to cover the critical frequency range (nominally 100 MHz to 3 GHz) of interest to lunar Cherenkov observations, and a different assumed observation time.

## 7.3 Expected Event Rates

In Table 4 we give the number of events expected per calendar year for the UHE neutrino flux models in Fig. 8 and the future lunar Cherenkov experiments we have simulated. The first of these possible experiments to become available will be with ATCA, with the completion of the CABB (Compact Array Broadband) upgrade in 2009. Since the dishes are relatively large (22 m), the antenna beam pattern cannot cover the Moon uniformly at high frequencies, though we find that a limb-pointing configuration (utilising the full bandwidth of 1-3 GHz) is optimal only at energies fractionally above the minimum detectable. Since the applicable energy range is so small, and the effective aperture in this range less than 0.1 km$^2$, we exclude a limb-pointing configuration from our analysis. In centre-pointing configuration, utilising the full bandwidth still yields the greatest aperture near threshold, though above $10^{20}$ eV, the optimal peak frequency $f_{max}$ is below 2 GHz. Though this experiment actually offers a lower collecting area than the Parkes experiment, this is more than compensated for by the large bandwidth and ability to simultaneously cover the entire visible lunar surface near 1 GHz, and we find an improvement of approximately an order of magnitude in both threshold and aperture is expected.

ASKAP, due to be completed in approximately 2011, offers up to twice the aperture of ATCA — due to a lower observation frequency — but with a similar threshold. The relative utility of each instrument as an UHE neutrino detector will probably therefore be determined by other considerations, such as ability to utilise existing processing power for de-dispersion (likely favouring ASKAP), usefulness as a platform to develop technologies scalable to the SKA (also

likely favouring ASKAP), and competition for observation time (favouring ATCA). Either of these two instruments will be able to improve on existing limits from RICE and ANITA-lite in the $10^{20}$–$10^{23}$ eV range in approximately two calendar months. While the expected number of events per calendar year is negligible for most of the production models (see Table 4), such observations would be sensitive to TD models considered by Protheroe & Stanev [58], and the larger flux estimates allowed under the generic optically thin AGN photoproduction models of Mannheim, Protheroe & Rachen [61].

As expected, the SKA offers a further leap forward in both threshold and sensitivity beyond the capabilities of ATCA or ASKAP. The three technology bands (dishes, low- and high-frequency AAs) are complementary, with the highest aperture from the low-frequency AA above $10^{20}$ eV, and from the dishes below $3 \times 10^{19}$ eV. The sensitivity of the high-frequency AA band (0.2-1 GHz) is somewhat reduced since the contribution to total system temperature from lunar thermal emission incident on a 60 m diameter cluster of AA tiles is significant. To a lesser extent this is true for the dishes, but in the low AA band (70–200 MHz), the Moon will actually appear colder than the sky due to rising galactic noise.

An apparent contradiction is that the estimated limits from LOFAR of Scholten et al. [21] are in fact stronger above $10^{22}$ eV by a factor of 2 than those for the SKA low-frequency AA, which will have a greater collecting area over the frequency range, and thus *must* be able to set the stronger limit. We emphasise that this factor is explained by differences in the modelling — we have run our simulation using the authors' reported techniques, and found agreement within the limits of our ability to reproduce their methods. The primary reason for our more pessimistic result is that the regolith substrate used here is a less efficient producer and transmitter of coherent Cherenkov radiation than the uniform regolith of Scholten et al., while numerous other differences in simulation techniques, e.g. our inclusion of surface roughness, are secondary effects. We would therefore argue that the LOFAR curve should sit entirely above that presented here for the SKA low-frequency AA.

The sensitivity provided by the SKA over all technology bands will allow most predictions of the GZK flux of UHE neutrinos to be probed in a single calendar year, with the sole exception being the model of Anchordoqui et al. [57]. The remaining GZK models will need as little as 1 month (Protheroe & Johnson [53], $E_{\max} = 3 \times 10^{21}$ eV) or as many as 18 months (Engel [55], EdS) to be detected / ruled-out at 90% confidence. Importantly, the flux of UHE neutrinos at energies detectable in the sub-regolith is predicted to be very low in all GZK models, with such events contributing at most 10% of the simulated detections, so that the detectability of the GZK flux is insensitive to the nature of the sub-regolith layer. For models (particularly TD models) predicting a large flux of neutrinos at the highest energies, the nature of the sub-regolith becomes very significant, and event rates could be as large as ten per day. The huge variation in the event rates — over four orders of magnitude — reflects both the current uncertainty in UHE CR origin, and the size of the parameter space which the SKA will be able to explore.

Of particular interest is the relative importance of the three SKA technology bands, with the band exhibiting the highest individual event rate being dependent on the flux models. Models where the low-frequency AA will have the highest event rate predict large fluxes of neutrino signals in all frequency bands, and will also be (at least marginally) detectable by both ATCA and

ASKAP, suggesting observations below 200 MHz, purely in terms of model detection and/or elimination, will be less critical for UHE neutrino physics. Individually, only the dishes are likely to detect fluxes consistent with all predictions, bar that of Anchordoqui et al., in a calendar year. However, given the myriad other frequency-dependent issues associated with lunar Cherenkov observations which we have so-far ignored (see the discussion), we feel that at this stage it would be unwise to presume conclusions can be drawn as to which frequency band will be most important for UHE neutrino observations.

The energy range at which the SKA could set a dominant limit is almost identical to that of ANITA, reflecting the overlap in observation frequencies (ANITA observes between 200-1200 MHz) and the similar geometry of the two experiments. At energies below $3 \times 10^{18}$ eV (the approximate SKA detection threshold), the expected flux is high enough to be detected by both Auger and fixed-volume Antarctic experiments such as IceCube. So far, our analysis has been purely in terms of sensitivity to an isotropic flux of UHE neutrinos – we will delay a discussion of the arrival direction sensitivity to a subsequent paper.

# 8 UHE Cosmic Ray detection with the SKA

In calculating the effective apertures of lunar Cherenkov experiments to UHE CRs, we found the results for the two methods of generating surface slopes to diverge for frequencies above a few hundred MHz, making it impossible to obtain reliable estimates for ATCA, ASKAP, and the SKA dishes, while for the SKA high-frequency AA, the two methods gave values different by more than a factor of two below $10^{21}$ eV. We therefore only present results for the SKA AAs, and await developments in lunar surface roughness theory to determine if the sensitivity to UHE CR at higher frequencies is significant.

The conventional experiment currently with the largest UHE CR aperture is that of the Pierre Auger Observatory. Consisting of a single ~3000 km$^2$ site in Argentina, by 2020 (when the full SKA comes on-line), a second, perhaps larger site in the USA will probably have been completed, with up to 10,000 km$^2$ of area. Here we assume sensitivity to all events of zenith angle $< 60^\circ$, and 100% detection efficiency, giving the total aperture of both sites to be approximately 30,000 km$^2$ sr. For an even comparison, we again weight the aperture by the fractional on-time $\epsilon_{\rm on}$ (= 1 for Auger, and 0.288 for the SKA AAs). The resulting weighted effective apertures are plotted in Fig. 9.

Even using the lower bound for the SKA apertures, the SKA low-frequency AA could expect a higher CR event rate above approximately 60 EeV than the combined Auger observatories. Coincidentally, this is approximately the energy at which the most significant anisotropies in arrival directions have been observed by Auger [1]. Since the aperture increases rapidly with cosmic ray energy, the event rate will fall much more slowly than with a fixed-aperture experiment such as Auger. This will allow a greater proportion of CR at the very highest energies (with the lowest deflection by magnetic fields) to be observed, although consequently the rate will be more sensitive to the spectral index at the highest energies. Measurements of the UHE CR spectrum from Auger [65, 66] indicate a spectrum of $dN/dE \propto E^{-4.14\pm0.42}$ above $10^{19.6}$ eV,

giving an annual event rate for the SKA low-frequency AA above 56 EeV of between 260 (unfavourable surface slopes, spectral index $-4.56$) and 1050 (independent slopes, spectral index $-3.72$), with the contributions to the uncertainty from the surface slopes model and UHE CR spectrum approximately equal. For comparison, the rate for a $13,000$ km$^2$ total collecting area (i.e. including the future Northern Hemisphere array) Pierre Auger Observatory is between about 40 and 60 per calendar year (depending only on spectral index). For any given assumption of surface roughness and spectral index, the SKA low-frequency AA would detect at least $\sim 30$ times as many cosmic rays above 56 EeV as the current Southern Pierre Auger Observatory.

The uncertainty in the aperture of the SKA high-frequency AA is somewhat greater than that for the low-frequency AA. While the sensitivity surpasses that of the low-frequency AA mostly only at energies where the Auger aperture dominates, there is a regime near 40-60 EeV where the apertures are comparable. In this regime, the optimal observation band for the low-frequency AA covers the full instrumental range of 70–200 MHz, while that of the high-frequency AA is only 200–300 MHz, suggesting that there could be a significant advantage in simultaneously observing with both instruments, or pushing up the maximum frequency of the low-frequency AA to (say) 300 MHz.

It must be stated that we are not arguing the SKA in particular, or the lunar Cherenkov technique in general, as a replacement to ground-based UHE CR detectors. Even at the highest energies, the technique will not provide any compositional measure of the UHE CR flux, and the energy resolution will probably be poor compared to current methods. The attraction lies in its ability to gather unprecedented statistics on the arrival directions of the highest energy cosmic rays, enabling more accurate statistics in correlation studies with potential source distributions. We qualitatively describe methods for determining the arrival direction, and for distinguishing cosmic rays from neutrinos, elsewhere — see James et al. [67]. A shift towards using higher energy CR for correlation studies will increase the advantage of the SKA with respect to current detection techniques.

# 9 Discussion

There are two broad bases upon which the accuracy of our estimates can be questioned, the first being our ability to detect the natural (or 'Luna-given') rate of lunar Cherenkov signals from UHE particle interactions in the Moon, and the second being our calculations of the signals themselves.

Our results show the potential apertures and event rates for future radio instruments, corresponding to the limit of thermal noise. There are many technical hurdles to be overcome to achieve this, as discussed by McFadden et al. [68]. Limitations on beam-forming capacity impose a frequency-baseline constraint on real-time triggering if the entire Moon is to be observed, meaning that the full sensitivity could only be recovered by setting a high trigger rate and writing buffered data from long baselines upon triggering. Coherent de-dispersion of the signal (which gets dispersed by the Earth's ionosphere, greatly reducing the peak strength) must be performed in real time prior to triggering, and this requires both specialised hardware

and a very accurate knowledge of the ionosphere. The baseline limitation is most restricting at high frequencies, the de-dispersion at low frequencies. Perhaps the greatest restriction will be obtaining significant observation time to perform UHE particle physics on a radio instrument. In this regard, the SKA AAs are least restrictive, since there is the possibility of forming multiple independent beams and carrying out lunar Cherenkov observations simultaneously with conventional radio astronomy by other telescope users.

There are three dominant sources of uncertainty in our calculations of radio-signals from UHE particle interactions in the outer layers of the Moon. The UHE neutrino-nucleon cross-section is very poorly constrained at such high energies even within the bounds of standard particle physics. To first order, the effective experimental aperture scales linearly with this cross-section, and a reduced cross-section may render some production models undetectable even with the SKA. Also, it is unlikely lunar Cherenkov experiments alone will break the degeneracy between flux normalisation and cross-section except perhaps with a very large number of detections. In combination with other experiments however, the prospects are promising, and we view determining the unknown cross-section as a scientific goal, rather than a theoretical limitation.

Our model of the regolith depth and sub-regolith layer is relatively poorly constrained by current observations, and could change with data from the next generation of lunar orbiters. Our calculated apertures from low-frequency (i.e. AA-low and AA-high) observations of UHE neutrinos only are sensitive to the existence or otherwise of such a layer, as radiation at high frequencies cannot escape from great depth, and cosmic rays interact near the surface. The (high-frequency) SKA dishes dominate the expected event rates given in Table 4 for most models of a UHE neutrino flux, and the exceptions are those where we expect a high event rate from all detectors from all modelled experiments. Therefore the question of regolith depth and sub-regolith structure is of less importance.

The main area in which the theory is under-developed is that of lunar surface roughness. Even at low frequencies, our method to put bounds on the aperture to UHE CR still allows a factor of three uncertainty in the case of the high frequency AA at 50 EeV, and prevented accurate modelling at higher frequencies. Also, our lower bound is not a physically rigorous bound in the strictest sense of the term. Obscuration of outgoing radiation by large-scale surface features ('self-shadowing') — a closely related problem — should also be included. Small-scale surface roughness, which could affect the coherence of radiation over the shower length, especially at high frequencies where the Moon is rougher, has so far been ignored, or treated as large-scale roughness. We hope to address these issues in a future paper.

We have shown that the SKA could utilise the lunar Cherenkov technique to detect the UHE neutrino flux above $3 \times 10^{18}$ eV under a wide range of production models, and provide unprecedented statistics on the flux of $> 50$ EeV cosmic rays. Both ATCA and ASKAP could detect or eliminate the most optimistic UHE neutrino production models in a reasonable observation time, though we cannot estimate their utility as cosmic ray detectors.

While the lunar Cherenkov technique alone can not perform all the science associated with UHE neutrino or CR observations, the next generation of radio-instruments will in the near-future be able to make significant contributions to each.

# Acknowledgments

We wish to thank J. Alvarez-Muñiz for his advice on the production of coherent Cherenkov radiation in different media, and also R. D. Ekers and R. A. McFadden for their advice on the challenges of using radio instruments for nanosecond pulse detection. This research was supported under the Australian Research Council's Discovery Project funding scheme (project number DP0559991).


# References


[1] The Pierre Auger Collaboration (Abraham et al.), Science 318 (2007) 938.

[2] K. Greisen, PRL 16 (1966) 748.

[3] G.T. Zatsepin, V.A. Kuzmin, JETP Lett. 4 (1966) 78.

[4] M. Takeda et al., Astropart.Phys. 19 (2003) 447.

[5] D.J. Bird et al., ApJ 441 (1995) 144.

[6] B.M. Connolly, S.Y. BenZvi, C.B. Finley, A.C. O'Neill, S. Westerhoff, Phys.Rev. D 74 (2006) 043001.

[7] T. Abu-Zayyad et al., Astropart.Phys. 23 (2005) 157.

[8] R.J. Prothroe, Astropart.Phys. 21 (2004) 415.

[9] P.W. Gorham et al., PRL 93 (2004) 041101.

[10] S.W. Barwick et al., PRL 96 (2006) 171101.

[11] R.J. Protheroe, R.W. Clay, PASA 21 (2004) 1.

[12] H. Falcke, P. Gorham, R.J. Protheroe, New Astron.Rev. 48 (2004) 1487.

[13] G.A. Askar'yan, Sov.Phys.JETP, 14 (1962) 441; 48 (1965) 988.

[14] D. Saltzberg et al., PRL 86 (2001) 2802.

[15] P.W. Gorham et al., Phys.Rev. D72 (2005) 023002.

[16] P.W. Gorham et al., PRL 99 (2007) 171101.

[17] J. Álvarez-Muñiz et al., Phys.Rev. D 68 (2003) 043001.

[18] R.D. Dagkesamanskii, I. M. Zheleznykh, Sov.Phys. JETP Let. 50 (1989) 233.

[19] T.H. Hankins, R.D. Ekers, J.D. O'Sullivan, MNRAS 283 (1996) 1027.

[20] A.R. Beresnyak, R.D. Dagkesamanskii, I.M. Zheleznykh, A.V. Kovalenko, V.V. Oreshko, Astronomy Reports 49 (2005) 127.

[21] O. Scholten et al., Astropart.Phys. 26 (2006) 219.

[22] E. Zas, F. Halzen, T. Stanev, Phys.Rev. D 45 (1992) 362.

[23] J. Alvarez-Muñiz, E. Zas, AIP Conf.Proc. 579 (2001) 128.

[24] P.W. Gorham, K.M. Liewer, C.J. Naudet, D.P. Saltzberg, D.R. Williams, presented at RADHEP 2000, arXiv:astro-ph/0102435 (2001).

[25] A.R. Beresnyak, arXiv:astro-ph/0310295v2 (2004).

[26] C.W. James, R.M. Crocker, R.D. Ekers, T.H. Hankins, J.D. O'Sullivan, R.J. Protheroe, MNRAS 379 (2007) 3.

[27] S. Johnston et al., PASA 24 (2007) 174. See also www.atnf.csiro.au/projects/askap/

[28] R.M. Crocker, F. Melia, R.R. Volkas, ApJ Lett., 622 (2005) L37

[29] R. Gandhi, C. Quigg, M.H. Reno, I. Sarcevic, Phys. Rev. D, 58 (1998) 093009

[30] M.K. Shepard, R.A. Brackett, R.E. Arvidson, JGR 100 (1996) 11709.

[31] O.Scholten et al., arXiv:astro-ph/0508580v2 (2005).

[32] B.B. Wilcox, M.S. Robinson, P.C. Thomas, B.R. Hawke, Meteoritics & Planetary Science 40 (2005) 695.

[33] M.A. Wieczorek, R.J. Phillips, JGR 103 (1998) 1715.

[34] G. Olhoeft, D. Strangway, Earth Planet.Sci.Lett. 24 (1975) 394.

[35] P.G. Lucey, G.J. Taylor, E. Malaret, Science 268 (1995) 1150.

[36] H.R. Aggarwal, V.R. Oberbeck, Lunar and Planetary Science Conference 10 (1979) 2689.

[37] K.L. Rasmussen, P.H. Warres, Nature 313 (1985) 121.

[38] T. Ono, H. Oya, Earth, Planets, and Space 52 (2000) 629.

[39] Y. Takano, Y. Takizawa, S. Sasaki, Acta Astronautica 57 (2005) 112.

[40] J. Alvarez-Muñiz, E. Zas, Phys.Lett. B 434 (1998) 396.

[41] J. Alvarez-Muñiz, R. Engel, T.K. Gaisser, J.A. Ortiz, T. Stanev, Phys.Rev. D 69 (2004) 103003.

[42] J. Alvarez-Muñiz, E. Zas, Phys.Lett. B 411 (1997) 218.

[43] D.R. Williams, The Askaryan Effect and Detection of Extremely High Energy Neutrinos in the Lunar Regolith and Salt, Dissertation, University of California (2004).

[44] W.-M.Yao et al. (Particle Data Group), J.Phys. G 33 (2006) 1.

[45] J. Alvarez-Muñiz, Phys.Rev. D 74 (2006) 023007.

[46] V.S. Troitskij, T.V. Tikhonova, Izv.Vyssh.Uchebn.Zaved.Radiofiz. 13 (1970) 1273.

[47] ATCA Observing Characteristics Calculator, www.atnf.csiro.au/observers/docs/at_sens/

[48] www.skatelescope.org

[49] P.W. Gorham, K.M. Liewer, C.J. Naudet, D. Saltzberg, D.R. Williams, arXiv:astro-ph/0102435 (2001).

[50] N.G. Lehtinen, P.W. Gorham, Phys.Rev. D 69 (2004) 013008.

[51] A. Ishihara for the IceCube Collaboration, arXiv:0711.0353v1 [astro-ph] (2007).

[52] I. Kravchenko et al., Phys.Rev. D 73 (2006) 082002.

[53] R.J. Protheroe, P.A. Johnson, Astropart.Phys. 4 (1996) 253.

[54] J.P. Rachen, P.L. Biermann, Astron.Astroph. 272 (1993) 161.

[55] R. Engel, D. Seckel, T. Stanev, Phys.Rev. D 64 (2001) 093010.

[56] D. Allard, M. Ave, N. Busca, M.A. Malkan, A.V. Olinto, E. Parizot, F.W. Stecker, T. Yamamoto, JCAP 9 (2005) 5.

[57] L.A. Anchordoqui, H. Goldberg, D. Hooper, S. Sarkar, A.M. Taylor, Phys.Rev. D 76 (2007) 123008.

[58] R.J. Protheroe, T. Stanev, PRL 77 (1996) 3708.

[59] R. Aloisio, V. Berezinsky, M. Kachelrieß, Nuc.Phys. B Proc.Supp. 136 (2004) 319.

[60] V. Berezinsky, arXiv astro-ph/0509675 (2005)

[61] K. Mannheim, R.J. Protheroe, J.P. Rachen, Phys.Rev. D 63 (2001) 023003.

[62] G. Miele, S. Pastor, O. Pisanti, Physics Letters B 634 (2006) 137.

[63] The Pierre Auger Collaboration (J. Abraham et al.), arXiv:0712.1909v1 [astro-ph] (2007).

[64] www.skads-eu.org

[65] T. Yamamoto (for the Auger Collaboration), arXiv:0707.2638v1 [astro-ph] (2007).

[66] M. Roth (for the Auger Collaboration), arXiv:0706.2096v1 [astro-ph] (2007).

[67] C.W. James, R.D. Ekers, R.A. McFadden, R.J. Protheroe, presented at the 30$^{th}$ ICRC, Merida, Mexico (2007); arXiv:0709.0160v1 [astro-ph].

[68] R.A. McFadden, R.D. Ekers, C.W. James, D. Jones, P. Roberts, R.J. Protheroe, presented at the 30$^{th}$ ICRC, Merida, Mexico (2007); arXiv:0801.3304v1 [astro-ph].

| $r$ (km) | 0–500 | 500–1000 | 1000–1670 | 1670–1749.99 | 1749.99–1750.00 |
|---|---|---|---|---|---|
| $\rho$ (g cm$^{-3}$) | 8.11 | 3.81 | 3.40 | 3.00 | 1.80 |

Table 1: The values of lunar density, scaled to give the correct lunar mass [43].

| Medium | $n$ | $\ell$ | $\theta_C$ | $\rho$ | $V_0$ | $f_0$ | $C_{\rm EM}$ | $C_H$ | $E_{\rm LPM}$ |
|---|---|---|---|---|---|---|---|---|---|
| Regolith | 1.73 | $60\lambda$ | 54.7° | 1.8 | 0.0845 | 2.32 | 4.57° | 2.40° | $7.70 \times 10^{-4}$ |
| Sub-Regolith | 2.5 | $29\lambda$ | 66.4° | 3.0 | 0.0569 | 2.38 | 4.69° | 2.46° | $4.64 \times 10^{-4}$ |

Table 2: Shower and radio Cherenkov parameters of the regolith and sub-regolith used in the present simulations. Units: $\rho$ (g/cm$^3$), $V_0$ (V/MHz), $f_0$ (GHz), $E_{\rm LPM}$ (EeV).

| Instrument | | $D$ (m) | $N$ | $S_0$ (m$^2$/K) | $f_{\rm min}$ (GHz) | $f_{\rm max}$ (GHz) |
|---|---|---|---|---|---|---|
| Parkes | Hi | 64 | 1 | 69 | 1.475 | 1.575 |
| | Lo | | | | 1.275 | 1.375 |
| GLUE | DSS14 LCP | 70 | 1 | 82.5 | 2.18 | 2.22 |
| | DSS14 RCP Hi | | | | 2.2 | 2.275 |
| | DSS14 RCP Lo | | | | 2.125 | 2.2 |
| | DSS13 Hi | 34 | 1 | 20.5 | 2.2 | 2.275 |
| | DSS13 Lo | | | | 2.125 | 2.2 |
| Kalyazin | | 64 | 1 | 69 | 2.25 | 2.35 |
| ATCA | | 22 | 6 | 61 | 1 | 3 |
| ASKAP | | 12 | 30 | 77.6 | 0.7 | 1.8 |
| SKA | AA Low | 60 | 154 | 4000 | 0.07 | 0.2 |
| | AA High | 60 | 154 | 10000 | 0.2 | 1 |
| | Dishes | 15 | 2476 | 10000 | 0.7 | 3 |

Table 3: Parameters of radio instruments used in the modelling of both past and future lunar Cherenkov experiments. Respectively, these parameters are dish diameter / AA cluster size $D$ (m), number of AA tile clusters or dishes $N$, base sensitivity $S_0$ (= $A_{\rm eff}/T_{\rm sys}$) before accounting for lunar emission, and frequency range of the instruments (triggering frequencies will in general be more restricted for the future experiments). The frequency range is also the maximum bandwidth, except for ASKAP which will have a maximum bandwidth of 300 MHz. For GLUE, when in defocused mode, DSS14 was treated as DSS13 in terms of $D$ and $S_0$.

| Author | Model | ATCA | ASKAP | AA-low | AA-high | Dishes | Full SKA |
|---|---|---|---|---|---|---|---|
| PS96 | | 20 | 40 | 3140 | 950 | 290 | 3200 |
| | | 10 | 14 | 240 | 108 | 73 | 266 |
| ABK04 | | 1.6 | 3.3 | 180 | 90 | 49 | 206 |
| | | 1.0 | 1.5 | 21 | 16 | 19 | 34 |
| PJ96 | $3 \times 10^{20}$ eV | 0 | 0 | 0.1 | 1.5 | 6.3 | 6.4 |
| | | 0 | 0 | 0.06 | 1.0 | 5.2 | 5.2 |
| | $3 \times 10^{21}$ eV | 0.18 | 0.33 | 9 | 18 | 29 | 35 |
| | | 0.16 | 0.23 | 2.6 | 7 | 18 | 19 |
| En01 | EdS | 0 | 0 | 0.03 | 0.3 | 1.7 | 1.7 |
| | | 0 | 0 | 0.01 | 0.2 | 1.5 | 1.5 |
| | $\Lambda$CDM | 0 | 0 | 0.04 | 0.5 | 2.9 | 2.9 |
| | | 0 | 0 | 0.02 | 0.34 | 2.5 | 2.5 |
| Al06 | $3 \times 10^{20}$ eV | 0 | 0 | 0.1 | 0.8 | 3.3 | 3.4 |
| | | 0 | 0 | 0.04 | 0.5 | 2.7 | 2.7 |
| | $3 \times 10^{21}$ eV | 0.18 | 0.35 | 21 | 12 | 11 | 30 |
| | | 0.11 | 0.17 | 2.3 | 3.0 | 6.4 | 7.9 |
| An07 | | 0 | 0 | 0 | 0.02 | 0.24 | 0.24 |
| | | 0 | 0 | 0 | 0.02 | 0.22 | 0.22 |
| MRP | $3 \times 10^{20}$ eV | 0.02 | 0.03 | 0.6 | 5.7 | 18 | 18 |
| | | 0.02 | 0.02 | 0.3 | 3.4 | 14 | 14 |
| | $10^{21}$ eV | 0.29 | 0.52 | 12 | 36 | 59 | 66 |
| | | 0.27 | 0.4 | 4.4 | 16 | 37 | 38 |
| | $3 \times 10^{21}$ eV | 2.6 | 5.0 | 156 | 194 | 182 | 293 |
| | | 2.2 | 3.3 | 38 | 58 | 88 | 105 |
| | $10^{22}$ eV | 14 | 28 | 1220 | 820 | 480 | 1480 |
| | | 10 | 15 | 190 | 170 | 180 | 300 |

Table 4: Expected number of neutrino events per calendar year from lunar Cherenkov experiments for the different models of the UHE neutrino flux plotted in Fig. 8, including (upper value) and excluding (lower value) the sub-regolith. A '0' implies an expected annual event rate of less than 0.05. The three SKA technology bands have been estimated separately, with the total calculated using the highest aperture at a given energy.

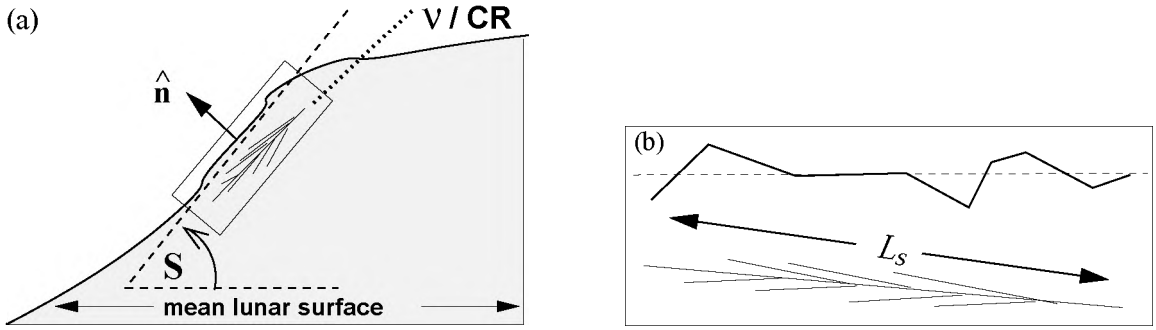


Figure 1: Surface roughness is described by the angular deviation $S$ of the local surface from the (horizontal) mean lunar surface, assuming a perfectly spherical moon. (a) Large-scale roughness approximation is illustrated where $S$ is taken to be constant over the length of the shower. (b) illustrates small-scale roughness where $S$ varies significantly over the length of the shower, $L_s$.

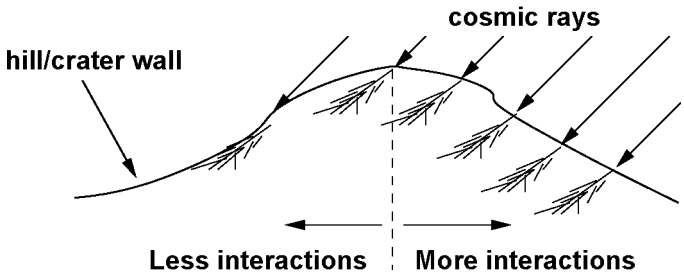


Figure 2: Cosmic rays will tend to interact on the sides of hills where the local surface normal is parallel to the arrival direction, so that the shower develops pointing away from the surface, reducing the probability that radiation from near the Cherenkov angle will escape.

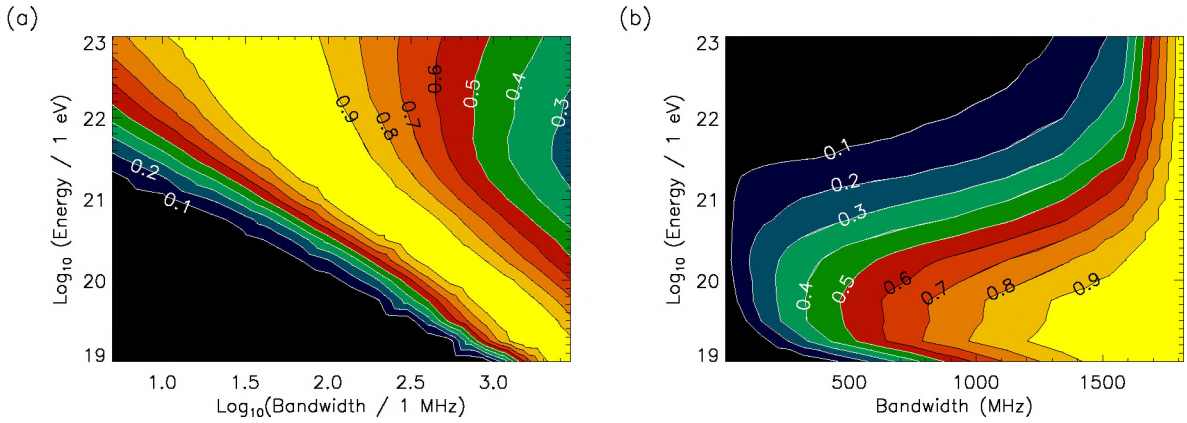


Figure 3: Contour maps of the normalised aperture $A(E_\nu, \Delta f)/A_{\max}(E_\nu)$ of a fictitious experiment (see text) to UHE neutrinos. (a) for $f_{\min}$ = 100 MHz, (b) for $f$ = 1 GHz.

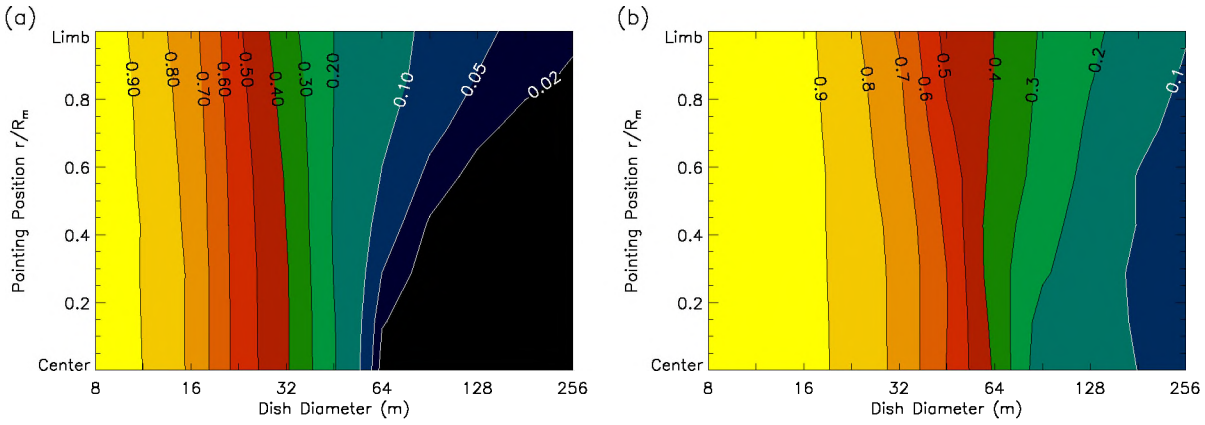


Figure 4: Contour maps of the effective aperture of a fictitious experiment (see text) to UHE neutrinos at energies of (a) $10^{20}$ eV and (b) $10^{22}$ eV, as a function of individual antenna diameter and pointing position. Contour levels are labelled as fractions of the peak aperture, achieved in each case for the centre-pointing mode of the minimum antenna diameter of 8 m.

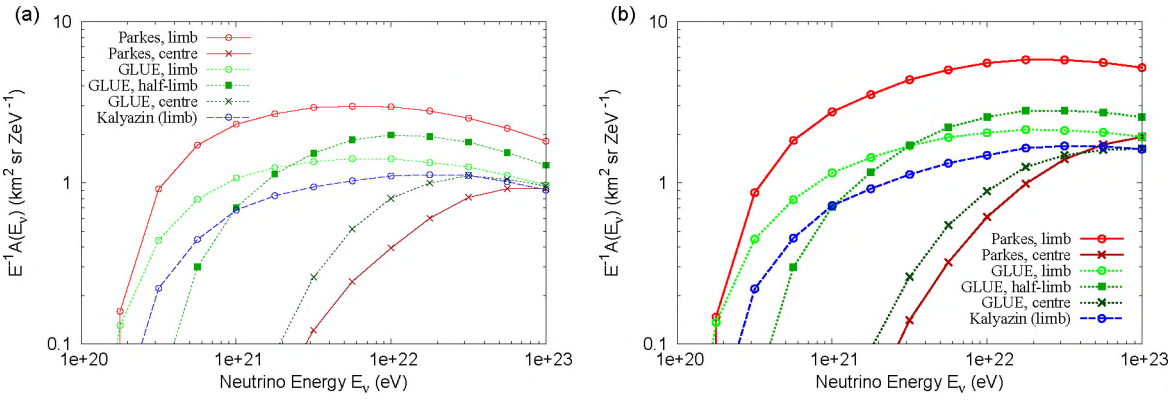


Figure 5: Effective apertures to UHE neutrinos of past lunar Cherenkov experiments, divided by neutrino energy in ZeV (1 ZeV = $10^{21}$ eV), both (a) excluding and (b) including the sub-regolith layer.

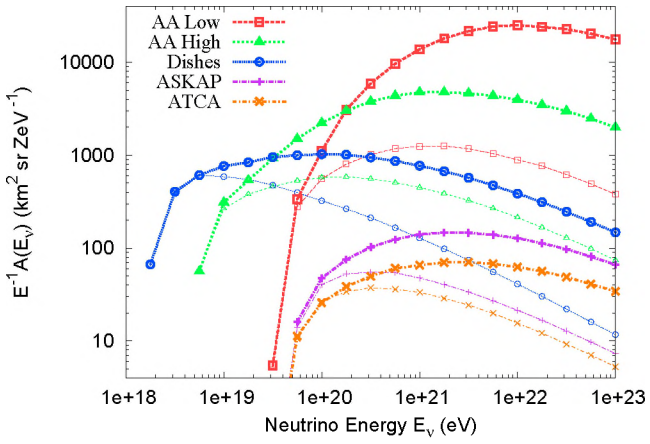


Figure 6: Effective apertures to UHE neutrinos of future lunar Cherenkov experiments, divided by neutrino energy in ZeV (1 ZeV = $10^{21}$ eV), both including (upper, thicker curves) and excluding (lower, fainter curves) the sub-regolith layer.

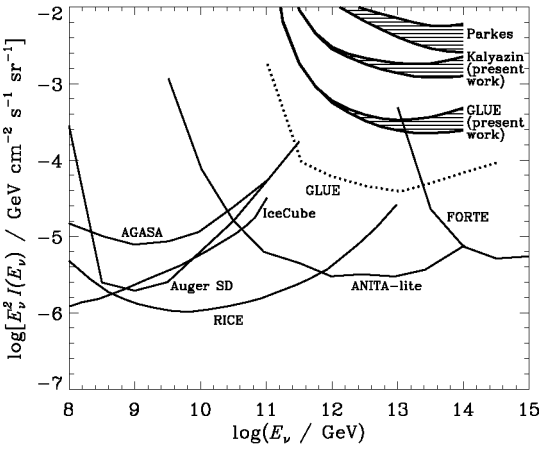


Figure 7: Existing model-independent limits on a total UHE neutrino flux (adjusted for all neutrino flavours) (see text) from: GLUE [9]; IceCube [51]; RICE [52]; ANITA-lite [10]; FORTE [50]; our revised estimates for Parkes, GLUE, and Kalyazin are shown by hatched bands (upper boundary – limit for 10 m regolith; lower boundary – 10 m regolith plus 2 km sub-regolith); Auger surface detectors [63].

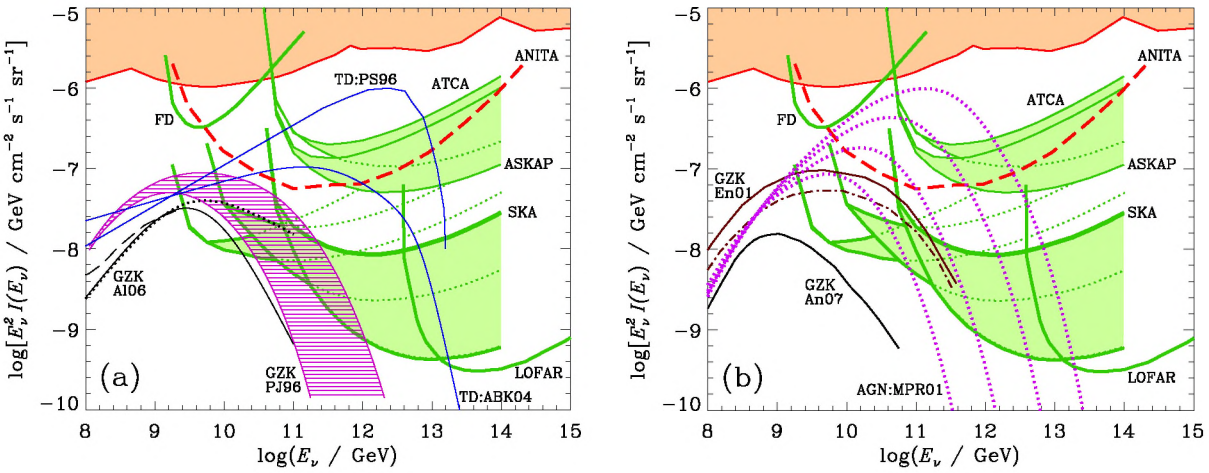


Figure 8: (a) and (b). Models of UHE neutrino production from GZK interaction: PJ96–Protheroe & Johnson [53] as expected for UHE CR acceleration in Fanaroff-Riley II radio galaxies [54] with protons accelerated with $E^{-2}$ spectrum to $3 \times 10^{11}$ and $3 \times 10^{12}$ GeV; En01–Engel et al. $E^{-2}$ spectrum to $3 \times 10^{12}$ (dashed– EdS cosmology; solid– $\Lambda$CDM cosmology) [55]; Al06–Allard et al. [56] with protons accelerated with $E^{-2.4}$ spectrum to $3 \times 10^{11}$ GeV (dashed), mixed composition with $E^{-2.1}$ to $Z \times 3 \times 10^{11}$ GeV (solid), and mixed composition with $E^{-2.1}$ spectrum to $Z \times 3 \times 10^{12}$ GeV (dotted); An07– Anchordoqui et al. [57] with protons accelerated with $E^{-2.2}$ spectrum to $4 \times 10^{11}$ GeV. Topological defects (TD) by: PS96–Protheroe & Stanev [58], ABK04–Aloisio, Berezinsky & Kachelreiß [59] (see [60]). Optically thin AGN photoproduction sources MPR01 with protons accelerated to $3 \times 10^{11}$, $10^{12}$, $3 \times 10^{12}$ and $10^{13}$ GeV, based on Fig. 2b of Mannheim, Protheroe & Rachen [61]. The limit on the total flux of UHE neutrinos (adjusted for all neutrino flavours) is plotted as the region excluded by past experiments (shaded area at top). The projected ANITA limit from their 2006 experiment [10] (adjusted for balloon flight duration), and predicted sensitivity for one calendar year of operation of future experiments to a flux of UHE neutrinos (adjusted for all neutrino flavours): 'FD' Auger Fluorescence Detectors [62]; LOFAR [21]; shaded bands (upper boundary – limit for 10 m regolith; lower boundary – 10 m regolith plus 2 km sub-regolith) from present work are shown for ATCA, ASKAP, SKA (left – dishes, middle – mid-frequency AA, right – low-frequency AA). The sensitivity for the mid-frequency AA is only shown as a shaded band where it is lower than the low-frequency AA shaded band and elsewhere is shown by thin dotted lines. Similarly, the sensitivity for the dishes is only shown as a shaded band where it is lower than the mid-frequency AA shaded band and elsewhere is shown by thin dotted lines.

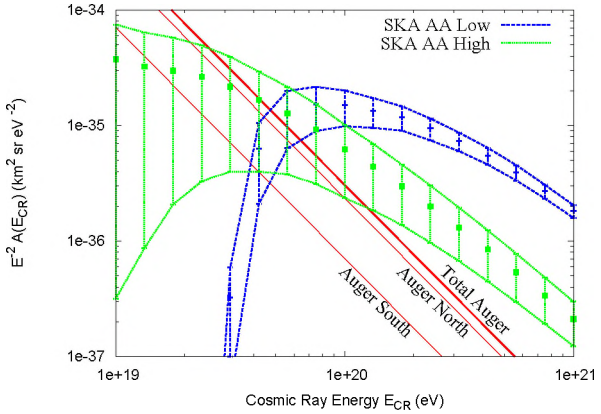


Figure 9: Comparison of the weighted effective aperture (effective aperture multiplied by fractional on-time) to cosmic rays of the SKA Aperture Arrays (high and low) with that of a potential 2020 Pierre Auger project ('Total Auger'), assuming a Northern site ('Auger North') of 10,000 km$^2$ in addition to the current observatory ('Auger South'). The upper and lower bounds come from calculations respectively assuming independent and unfavourable surface slopes.